Imaging of Thermal Effects during High-Intensity Ultrasound Treatment in Liver by Passive Elastography: A Preliminary Feasibility in Vitro Study

Victor Barrere, David Melodelima, Stefan Catheline, Bruno Giammarinaro

Version of Record: https://www.sciencedirect.com/science/article/pii/S0301562920301356
Manuscript_0183cc1311e2dd2769c8d335d20ecdcd

Imaging of thermal effects during high-intensity ultrasound treatment in liver by passive elastography: a preliminary feasibility *in-vitro* study

V. Barrère[a], D. Melodelima[a], S. Catheline[a,*], B. Giammarinaro[a]

[a]*LabTAU, INSERM, Centre Léon Bérard, Université Lyon 1, Univ Lyon, F-69003, LYON, France*

Abstract

High-intensity focused ultrasound is a noninvasive modality for thermal ablation of tissues through locally increased temperature. Thermal lesions can be monitored by elastography, following the changes in the elastic properties of the tissue as reflected by the shear-wave velocity. Most studies on ultrasound elastography use shear waves created by acoustic radiation force. However, in the human body, the natural noise due to cardiac activity or arterial pulsatility can be used to characterize elasticity through noise-correlation techniques, as the method known as passive elastography. The objective of this study was to investigate the feasibility of monitoring high-intensity ultrasound treatments of liver tissue using passive elastography. Bovine livers were heated to 80 °C using a high-intensity planar transducer, and imaged with a high-frame-rate ultrasound imaging device. The dynamics of lesion formation are captured through tissue stiffening and lesion expansion.

Keywords: Ultrasound, Elastography, Shear waves, Diffuse wavefield,

*Corresponding Author: Stefan Catheline, 151 cours Albert Thomas 69424 LYON Cedex 03 France; Email, stefan.catheline@inserm.fr; Phone, +33475681943

Thermal ablation, Monitoring

Introduction

High-intensity focused ultrasound (HIFU) allows noninvasive creation of thermal lesions in deep tissues, and therefore requires techniques to monitor lesion formation.

Today, magnetic resonance imaging (MRI) remains the gold standard for monitoring HIFU interventions in the clinic. This provides good anatomical images of tissues and lesions, as well as temperature maps during the interventions (Wu *et al.* , 2001). On the other hand, MRI is not portable, it is expensive, and it has patient and device compatibility issues. Some HIFU devices also integrate ultrasonic imaging. This modality is cheaper, more easily available, and more portable than MRI imaging (Ebbini & Ter Haar, 2015). This method allows acquisition with high spatial and temporal resolution that provides B-mode images as well as thermal mapping, along with the use of contrast agents to monitor the exposure after treatment. Techniques directly based on ultrasound measurements can be based on changes in the characteristics of the compression waves (Anand & Kaczkowski, 2004). Ultrasound thermometry has also been investigated using various ultrasound characteristics, such as the speed of sound (Bayat *et al.* , 2015), the nonlinearity coefficient B/A (Choi *et al.* , 2011), and the backscattered coefficient (Ghoshal *et al.* , 2016). However, to date, techniques based on changes in the speed of sound have been limited to temperatures below 55°C. The coefficient B/A appears to increase linearly as a function of temperature *in vitro*, although as it requires a transmission measurement device, it cannot be measured *in vivo* (Choi *et al.* , 2011). Ultrasound monitoring techniques based on backscattered signals have also been studied, such as backscattered

energy techniques, which have already been implemented for commercial devices (Sanghvi *et al.* , 2017; Zhou, 2017). However, so far, this technique allows for efficient monitoring, while it cannot be used for thermal measurements.

Alternatively, thermal lesions induce changes to the elasticity of a medium, thus allowing elastography to be used to monitor HIFU treatment. This method consists of measuring the shear-wave velocity, which is directly linked to the tissue elasticity. In this domain, the same difficulties as described above are found between magnetic resonance elastography and elastography using ultrasound imaging. Different techniques to observe and create shear waves have been described in the literature (Parker *et al.* , 2011; Tanter & Fink, 2014; Giammarinaro *et al.* , 2018). The most commonly used technique consists of using the acoustic radiation force to create a shear-wave source in the medium. Shear waves are then imaged using a high-frame-rate ultrasound scanner (Bercoff *et al.* , 2004). This technique has already been applied to muscle and liver, in 2010 by Sapin-de Brosses *et al.* (2010). Arnal *et al.* (2011) presented a method for shear-wave thermometry in different tissue samples, although this method was only accurate at temperatures below 55 °C.

Methods based on acoustic radiation force are limited when creating the required shear waves in deep tissues. However, the development of passive methods might solve this issue. The ability to perform elastography would mainly rely on the imaging technique for the shear-wave monitoring. Passive elastography was developed recently, and it is based on noise-correlation techniques. Noise-correlation techniques were first used in seismology to

retrieve impulse responses (Aki & Richards, 2002), and therefore the Green's function, in a medium (Sanchez-Sesma, 2006). These techniques have also been studied from a time-reversal point of view, in cavities and in open media (Derode *et al.* , 2002).

This method was applied to characterize muscle by Sabra *et al.* (2007), and it was modified for two-dimensional imaging by Gallot *et al.* (2011). Catheline *et al.* (2013) reported on a new algorithm to estimate the shear elasticity using high-frame-rate imaging (Sandrin *et al.* , 1999) and classical low-frame-rate imaging. This latter has also been used for the brain with MRI (Zorgani *et al.* , 2015), for the cornea with optical tomography (Nguyen *et al.* , 2016), and for cells (Grasland-Mongrain *et al.* , 2018). As passive elastography has only been developed recently, its feasibility for HIFU monitoring has not been investigated, to the best of our knowledge. In the literature, different organs have been studied for HIFU therapy, as reviewed by (Maloney & Hwang, 2015). The liver is an interesting organ to use for this feasibility study, because it is already a well-studied organ. It has been characterized in terms of elasticity through axial-shear-strain elastography (Thittai *et al.* , 2010), shear-wave elastography (Sapin-de Brosses *et al.* , 2010; Arnal *et al.* , 2011), and MRI (Righetti *et al.* , 1999). However, the most important point is that the *in-vivo* feasibility for passive elastography imaging of the liver has already been demonstrated by (Gallot *et al.* , 2011). This thus defined the objective of the present study, which was to evaluate the feasibility of monitoring thermal lesion formation in liver tissue from 37 °C to 80 °C by passive elastography. In this regard, this preliminary experimental study was performed with bovine liver, and with a planar transducer

as the treatment device. This study is thus devoted to evaluation of the feasibility of monitoring changes during high-intensity ultrasound treatment by imaging elasticity.

Material and methods

Experimental configuration. The set-up is illustrated in Figure 1, and it was built to perform high-intensity ultrasound treatments *in vitro*, with a planar transducer placed above the sample holder. An unfocused transducer was chosen to generate wide exposure, which is considered to be homogeneous at the imaged depth, and is slow enough to perform several imaging acquisitions during the treatment. The increased temperatures can be considered to be more homogeneous using this set-up. A linear transducer array that is connected to a high-frame-rate ultrasound scanner is positioned on the side of the sample holder, to image the tissue samples. The temperatures were monitored using a needle thermocouple (29/5; Physitemp Instruments LLC, Clifton, NJ, USA) positioned just above the center of the imaging plane. The experiments were performed in a water-filled tank. The water was degassed, and homogeneously heated to 37 °C using a thermostat (Polystat 36; Fisher Scientific, Hampton, NH, USA), to mimic the physiological conditions of the human body. The thermostat was turned off during interventions to avoid the creation of global motion of the sample through water waves. An external shaker (Model K2004E01; The Modal Shop Inc., Cincinnati, OH, USA) was used to simulate a diffuse wavefield in the tissues samples. Each aspect of the experimental procedures is described further in the following sections.

Tissue preparation. Bovine livers were collected from a local slaughter house. They were sliced into rectangular prisms of 10 cm x 3 cm x 6 cm with a scalpel, and then stored in a freezer. The pieces of liver tissue were defrosted in a fridge 1 day before each experiment. For each intervention, each tissue sample was placed in degassed water with 4 mg/L oxygen, and degassed in a vacuum chamber for 45 min. The aim was to avoid the formation of hyperechogenic microbubbles within the tissue (Bamber & Hill, 1979). A tissue sample was then placed in a custom-made holder, with measurements taken with a multi-element ultrasound imaging probe (L7-4; Philips, Amsterdam, The Netherlands) coupled to the ultrasound system (Vantage 256; Verasonics, Kirkland, WA, USA).

Lesion formation. The temperature increases were generated by a 3-MHz home-made piezo-composite plane transducer with a circular effective surface of 126 mm^2. The probe was powered by a signal generator (programmable 15-MHz function generator HM8131-2; Hameg Instruments, Mainhausen, Germany) which was amplified by a 55-dB power amplifier (41501; ADECE, Artannes, France). An acoustic power of 2.4 W was emitted by the therapy probe. The energy of the amplified signal supplied to the probe was monitored with a wattmeter (power reflection meter NAP; Rohde & Schwartz, Munich, Germany). The temperature of the transducer was controlled by a cooling system (Ablapack & Ablasonic, Edap TMS, Vaulx-en-Velin, France) that included a peristaltic pump (model 7518-60; Masterflex, Béligneux, France) and a minichiller (RC6; LAUDA-Brinkmann, LP., Delrann NJ, USA). The temperature in the tissue sample increased from 37 °C up to 80 °C. The average increase in temperature was 3 °C/min. The tissue was then allowed

to cool down naturally to 40 °C. The heating was interrupted for 7 s every minute to perform the ultrasonic acquisitions (see Figure 2).

Passive elastography and imaging. Shear-wave velocity measurements were performed using a method developed by Catheline *et al.* (2013), as modified for the present study (see Appendix). This was based on a time-reversal technique that is also known as 'noise correlation', which allows for the retrieval of the Green's function from a diffuse wavefield (Sanchez-Sesma, 2006).

This technique requires the image acquisition to be at a high enough frame rate to meet Shannon's criterion. An ultrasound scanner (Vantage 256; Verasonics, Kirkland, OH, USA) was used, which was coupled to a linear transducer array (L7-4; Philips, Amsterdam, The Netherlands). The ultrasound scanner was fully controlled using Matlab 2013a (Mathworks, Natick, MA, USA). An empirical numerical apodisation A was applied to the 128 elements using the Matlab function *tukeywin*, such that:

$$A = 0.5 * tukeywin(128, 0.2) + 0.5.$$

Each imaging sequence was composed of 300 images. These were acquired at 600 frames/s from plane waves (Sandrin *et al.* , 1999) emitted at five different angles between $\pm 10°$, to perform the compounding method (Montaldo *et al.* , 2009). At the beginning of each sequence, the external shaker received a synchronizing trigger signal from the ultrasound scanner. This emitted a sinusoidal signal that lasted 1 s, at a frequency of 60 Hz for a voltage of 1 V peak to peak. This frequency was chosen to be in the frequency bandwidth measured in previous liver experiments (Gallot *et al.* , 2011). The ultrasound images were then stored as in-phase and quadrature (IQ) data and the Loupas

phase-based motion estimator (Pinton *et al.* , 2005; Lindop *et al.* , 2008; Deng *et al.* , 2017) was used to estimate the particle velocity of the tissue between each ultrasound image. The displacement calculations were performed over windows of two ultrasonic wavelengths. Therefore, for each elasticity map calculated, 300 ultrasound images were used to obtain 299 particular velocity maps. This method allowed the shear-wave velocity map to be obtained over approximately 30 s, and therefore to observe the elasticity changes during the treatment. The choice of 1 min between acquisitions was made based on the calculation times.

Results and Discussions

High-intensity treatments

The experiments were performed on eight bovine liver tissue samples. Each treatment resulted in the formation of a lesion that was macroscopically visible as a local color change of the tissue. The lesions created in the tissue samples were sliced along the imaging plane. Corresponding images are presented in the third column of Figures 3 and 4. The treated zones were harder to the touch, by palpation, than the untreated liver tissue. The images in Figures 3 and 4 also show that wide lesions (approximately 35 mm x 45 mm) were created using the unfocused plane transducer, as expected. Furthermore, the heat deposit appeared to be relatively homogeneous during the experiments, as the lesions were wide and relatively uniform. In several of the images taken immediately after the treatments, the exposure appeared lighter than the untreated area. A pink border was sometimes observed around the treated area just after the treatment, although this disappeared

after a couple of minutes. Chu & Dupuy (2014) explained that lesions *in vivo* are composed of a central zone, which corresponds to irreversible coagulative necrosis, and a peripheral zone that is subjected to sublethal damage, and which contains a large quantity of blood. The *in-vitro* phenomenon might be the result of damage before coagulation around the coagulated area, combined with blood expulsion from the exposed area. Moreover, this peripheral zone was also observed in the shear-wave velocity maps that are described in more detail in the following section.

Imaging method for the shear-wave field and time reversal

During the experiments, shear waves were created with an external vibrator that hit the sample holder. The vibration transmitted through the plastic structure perfectly propagated through the liver tissue as shear waves. The particle velocities due to these shear waves were then estimated using an ultrafast ultrasound scanner. A typical example of a shear-wave field is shown in Figure 5, where four time points are shown for a shear-wave front over 5 ms in sample 1. The shear-wave propagation through the sample can be seen over 500 ms with a frame rate of 600 Hz. Thus, using correlation, a coherence function (or time-reversed focal spot) was computed. The passive elastography algorithm consisted of studying the properties of this focal spot. Its size, or radius of curvature, is directly linked to the shear-wave wavelength (Brum *et al.* , 2008; Gallot *et al.* , 2011; Benech *et al.* , 2013). Figure 6 shows typical focal spots, where the location is estimated by the white cross for sample 3 before and after treatment. We can see that the focal spot becomes much larger, which indicates an increase in the shear-wave velocity in the treated tissue. The shapes of the focal spots greatly depend

on the elastic heterogeneities of the samples. The global expansion seen is in agreement with a global increase in elasticity.

The possibility of locally estimating the Green's function shape confirms this use of the passive elastography algorithm (summarized in Appendix). As a result, the shear-wave speed can be estimated for every point by moving the position (marked by a white cross) where the focal spot properties are calculated. This position corresponds to the pseudo-source $\vec{r}_0$, as defined in the Appendix in Equation 1. It should also be keep in mind that the wave-speed measurements are conducted in the vicinity of the focal spot maximum, where the signal-to-noise ratio is largest.

In this study, it is acknowledged that there is no natural noise, and thus the waves were created using an external shaker. During *in-vivo* experiments, natural noise arises due to cardiac activity and arterial pulsatility. This latter has already been used for the brain (Zorgani *et al.* , 2015). The shear waves presented here were created with a central frequency of around 60 Hz. In the literature, measurements have already been performed *in vivo* by (Gallot *et al.* , 2011). Moreover, during actual *in-vivo* experiments, respiratory motion needs to be taken into account, because this motion can lead to errors in the shear-wave speed estimation and map reconstruction.

Imaging by passive elastography during high-intensity treatments

Each experiment lasted approximately 1 h. Every minute during the heating and cooling periods, for a break of 7 s, the shear-wave velocity maps were computed using the passive elastography algorithm. These results are presented as Videos 1-8, which correspond to samples 1 to 8, respectively. Each movie is thus composed of all of the shear-wave velocity maps obtained

every minute over 45 min, and the temperature at the center of the image is indicated in the title of each frame. On top of this, the black line represents the whole region where the elasticity changes are visible.

In each movie, the tissue within the region of interest (ROI) appears to become stiffer during the heating phase, and more stable during the cooling phase. However, the thermal lesion formation is not always the same. Some movies show spatially uniform increases in the shear-wave velocity during the heating, which suggests that the heating was homogeneous. Other movies show tissue stiffness spreading over time from a point source. Throughout this spreading of the stiff region, a softer border can be seen. This phenomenon is shown in Figure 7, which shows three shear-wave velocity maps that were calculated every minute. It appears that on the first map, two stiffer parts were surrounded by softer borders, which eventually merged during the lesion formation. This phenomenon might have the same explanation as the pink border seen in the photographs presented in Figures 3 and 4. This border would indicate a softer part of the tissue during the experiment, and would still be observable immediately after the treatment.

Lesions detected by passive elastography

In the previous section, we showed the shear-wave velocity maps that were calculated during the treatments, where increases in velocity were seen. These shear-wave velocity maps before and after the treatments are shown in the first and second columns, respectively, of Figures 3 and 4.

For every sample, an increase in shear-wave velocity was seen, which is in agreement with Videos 1-8. With the exceptions of samples 5 and 6, the wide stiff regions appear to correspond to the lesions observed in the third

column of Figures 3 and 4. However, it is important to consider that the experimental ultrasound imaging planes might have been slightly different from the photographs presented in the previous sections. Despite our efforts, cutting through the samples to reveal a surface that perfectly coincided with the imaging plane was challenging. Contrary to other samples, samples 5 and 6 have no clear lesion in the photographs. However, the stiffness appears to be higher post-treatment than pre-treatment in these samples. This is an encouraging result for the feasibility of monitoring lesion formation. For every sample, an irreversible change was detected.

Average shear-wave velocity in the lesions

For all of the experiments, the ROIs displayed in Figures 3 and 4 were used to calculate the average shear-wave velocities on a minute-by-minute basis. These are displayed on the third column of Figures 3 and 4. With the ROIs selected afterwards, dynamic effects on the shapes of exposures were also involved in the average velocity change. The shapes and sizes of the ROIs changed as they were adapted to each observable lesion.

Similar tendencies can be observed for each sample. During the heating period, the shear-wave velocity was relatively stable, sometimes showing a small increase or decrease. From around 45°C, the shear-wave velocity was strongly modified, until the maximum temperature was reached for each experiment. During the subsequent cooling phase, a plateau was observed that corresponds to the final maps shown in the corresponding Figure. The stability of the velocities before reaching 45°C and the plateau after heating appear to show that the effects of the ultrasound are mainly irreversible effects that change the elasticity and nature of the soft tissues. These results

are consistent with experiments from Sapin-de Brosses *et al.* (2011) that showed similar tendencies for the evolution of the shear modulus as a function of the temperature.

However, some differences can be highlighted between the experiments. The first concerns the maximum temperature, which can be caused by different effects. First, although the ultrasound intensity was set to be constant, the shape of the samples varied. Thinner samples enhanced the heat exchange with the thermal bath, and were thus prevented from reaching higher temperatures in the tissue. Moreover, the blood vessels in the samples can prevent high temperature increases (see Figures 3 & 4). Indeed, the temperature increases are caused by tissue absorption. However, in the tissue, there are still some blood vessels and bile ducts, which are full of water here. If these are in the high-intensity ultrasound beam, less heat is generated by the ultrasound due to the weak absorption of this water. Moreover, this implies that the tissue is highly heterogeneous, with large impedance differences that can induce some large scattering effects, and thus beam deformations.

Another visible difference concerns the behavior observed for each curve. The general tendency previously described is well followed by samples 3, 4, 7, and 8. However, even though samples 1, 2, 5, and 6 followed the tendencies already reported in the literature, they present some variations in their behaviors. During the heating phase, the behavior was less monotonous, and it even corresponded to a decrease in the shear-wave velocity for samples 1 and 6.

These might be explained by tissue motion. During the temperature changes, the tissues suffer from mechanical deformation, such as dilatation

or contraction. Therefore, the measurements might have been performed under pre-stressed conditions (*i.e.*, stress created by the sample holder), which would modify the shear-wave velocity measured (Gennisson *et al.* , 2007) through acoustoelastic effects. Moreover, tissue deformation can induce motion of the sample, and therefore of the imaging plane. This might explain some of the movements observed in the movies and the discontinuity in sample 5. Another possibility to explain the differences between the experiments would be the dynamic effects: several lesions were created at the same time for sample 7, and they merged to form a single wider lesion. This highlights one of the advantages of the present technique, as it corresponds to imaging of the formation of the lesion, thus characterizing its spatio-temporal dynamics.

Furthermore, some differences can be observed between samples 4 and 8. The maximum measured temperatures were in both cases around 70°C, but the estimated shear-wave velocities were different. This might be explained by the position of the thermocouple, which might have induced some errors for the temperature estimation. This might also come from differences in the sample shapes, as previously indicated. Indeed, the maximum temperature might have been the same, but might not have been reached over the same duration of time.

Conclusions

In the present study, the aim was to investigate the feasibility of HIFU monitoring by passive elastography. As such, eight bovine liver tissue samples were treated *in vitro* by ultrasound. In each case, the experiments were

successfully imaged by passive elastography during the heating and cooling. Shear-wave velocity changes were observed during the lesion formation for a 4 x 4 cm^2 area. The imaging experiments allowed for observation of the physical changes during these treatments. The dynamics of the lesion formation were characterized: the creation of small lesions at different positions, which then spread in size over time until they fused into wider lesions. Other lesions showed individual expansion over time. Moreover, the imaged dynamics are similar to those described in the literature, as shown by the estimations of the average shear-wave velocities. These first results are encouraging for such imaging and characterization of the exposure generated by ultrasound in soft tissues. However, present experiments being *in vitro*, the *in-vivo* feasibility should be investigated further to allow for using natural vibrations , as well as the role of perfusion.

Appendix: The passive elastography algorithm

The method described here is based on the paper from Catheline *et al.* (2013) and uses a time-reversal method to estimate the shear-wave velocity in the medium. This algorithm is based on the possibility to retrieve the Green's function through noise correlation from a diffuse wavefield (Sanchez-Sesma, 2006).

Given a diffuse wavefield in an isotropic homogeneous solid measured along the z-axis, the respective displacement is $u_3(\vec{r},t) = \phi(\vec{r},t)$, where $\vec{r}$ is the position and t is the time. The corresponding time-reversed function is defined as the convolution over time by:

$$\Phi^{TR}(\vec{r}_0,\vec{r},\tau) = \phi(\vec{r}_0,-t) \otimes \phi(\vec{r},t). \quad (1)$$

With differentiation over the source point locations $\vec{r}_0$ and $\vec{r}$, the time-reversed field leads to:

$$\frac{\partial^2 \Phi^{TR}}{\partial \vec{r}_0 \partial \vec{r}} = \frac{\partial \phi}{\partial \vec{r}_0}(\vec{r}_0, -t) \otimes \frac{\partial \phi}{\partial \vec{r}}(\vec{r}, t) \tag{2}$$

Moreover, the time-reversed function $\Phi^{TR}(\vec{r}_0, \vec{r}, \tau)$ is linked to the Green's function, which only depends on $\vec{R} = \vec{r} - \vec{r}_0$ in a homogeneous and isotropic medium. This can be defined by $\Phi^{TR}(\vec{r}_0, \vec{r}, \tau) = \Phi^{RT}(\vec{R} = \vec{r}_0 - \vec{r}, \tau)$. This new definition implies that:

$$\frac{\partial^2 \Phi^{TR}}{\partial \vec{r}_0 \partial \vec{r}} = -\frac{\partial^2 \Phi^{TR}}{\partial \vec{R}^2}, \tag{3}$$

and therefore,

$$\frac{\partial^2 \Phi^{TR}}{\partial \vec{R}^2} = -\frac{\partial \phi}{\partial \vec{r}_0}(\vec{r}_0, -t) \otimes \frac{\partial \phi}{\partial \vec{r}}(\vec{r}, t). \tag{4}$$

Assuming a monochromatic wavefield, the time-reversal field is related to the Green's function in the Fourier domain by:

$$\tilde{\Phi}^{TR}(\vec{r}_0, \vec{r}, \omega) = \tilde{\phi}^*(\vec{r}_0, \omega)\tilde{\phi}(\vec{r}, \omega) \propto \mathrm{Im}\left[G_{33}(\vec{R} = \vec{r}_0 - \vec{r}, \omega)\right] \tag{5}$$

The described method is based on the near field of the Green's function, which can be approximated by Benech *et al.* (2013):

$$\tilde{\Phi}^{TR}(0, \vec{r}, \omega) \propto \frac{k}{12\pi\mu} \left\{ \left(\frac{\beta}{\alpha}\right)^3 \left(1 - \frac{(qr)^2}{10}\right) + 2\left(1 - \frac{(kr)^2}{5}\right) + \frac{1}{5}\left[(kr)^2 - \left(\frac{\beta}{\alpha}\right)^3\right] cos^2(\theta) \right\} \tag{6}$$

where μ is the shear modulus, α and β are the compression and shear-wave velocities, respectively, q and k are their respective wave numbers, and θ is the angle between the z-axis and $\vec{r}$.

Equation6 shows that the amplitude of the time-reversed field is related to:

$$\tilde{\Phi}^{TR}(0,0,\omega) \propto \frac{k}{6\pi\mu} \tag{7}$$

and for the case of the strain along a line:

$$-\frac{\partial^2\tilde{\Phi}^{TR}}{\partial R^2}(0,0,\omega) \propto (2-cos^2\theta)\frac{k^3}{30\pi\mu} \tag{8}$$

Considering the time-reversed strain function ζ_z^{RT} and ζ_x^{RT} defined in Catheline *et al.* (2013), respectively, along the z and x axes:

$$\tilde{\zeta}_z^{TR}(\vec{R}=0,\omega) \propto \frac{k^3}{30\pi\mu} \tag{9}$$

$$\tilde{\zeta}_x^{TR}(\vec{R}=0,\omega) \propto 2\frac{k^3}{30\pi\mu} \tag{10}$$

$$\tilde{\zeta}_z^{TR}(\vec{R}=0,\omega) + 2\tilde{\zeta}_x^{TR}(\vec{R}=0,\omega) \propto \frac{k^3}{6\pi\mu} \tag{11}$$

The time-reversed particle velocity is given by:

$$V^{TR}(\vec{r}_0,\vec{r},\tau) = \frac{\partial\phi}{\partial t}(\vec{r}_0,-t) \otimes \frac{\partial\phi}{\partial t}(\vec{r},t). \tag{12}$$

In using the derivative properties of the convolution, the previous equation results in the time-reversed particle velocity at position $\vec{r}_0$ being defined as:

$$V^{TR}(\vec{R}=0,\tau) = -\frac{\partial^2\Phi^{TR}}{\partial\tau^2}(\vec{R}=0,\tau) \tag{13}$$

and in the Fourier domain, it can be approximated by:

$$\tilde{V}^{TR}(\vec{R}=0,\omega) \propto \frac{\omega^2 k}{6\pi\mu} \tag{14}$$

Previous calculations were performed in the Fourier domain. However, under the assumption of a monofrequency signal, they are still accurate in the time domain. This leads to the possibility to estimate the shear-wave velocity as:

$$c = \frac{\omega}{k} = \sqrt{\frac{V_0^{TR}}{\zeta_z^{TR} + 2\zeta_x^{TR}}} \tag{15}$$

Acknowledgements

This study was supported by Banque Publique d'Investissement (PIA, PSPC 2015)

References

Aki, K & Richards, P. Quantitative seismology.. *Page 700 of: Book*. University Science Books. 2002

Anand, A & Kaczkowski, PJ. Monitoring formation of high intensity focused ultrasound (HIFU) induced lesions using backscattered ultrasound. *Acoustics Research Letters Online*, 2004, **5**(3), 88–94.

Arnal, B, Pernot, M & Tanter, M. Monitoring of thermal therapy based on shear modulus changes: II. Shear wave imaging of thermal lesions. *IEEE Trans Ultrason Ferroelectr Freq Control*, 2011, **58**(8), 1603–1611.

Bamber, JC & Hill, CR. Ultrasonic attenuation and propagation speed in mammalian tissues as a function of temperature. *Ultrasound Med Biol*, 1979, **5**(2), 149–157.

Bayat, M, Ballard, JR & Ebbini, ES. <italic>In Vivo</italic> Ultrasound Thermography in Presence of Temperature Heterogeneity and Natural Motions. *IEEE Trans Biomed Eng* , 2015, **62**(2), 450–457.

Benech, N, Brum, J, Catheline, S, Gallot, T & Negreira, C. Near-field effects in Green's function retrieval from cross-correlation of elastic fields: experimental study with application to elastography. *J Acoust Soc Am*, 2013, **133**(5), 2755–66.

Bercoff, J, Tanter, M & Fink, M. Supersonic shear imaging: a new technique for soft tissue elasticity mapping. *IEEE Trans Ultrason Ferroelectr Freq Control*, 2004, **51**(4), 396–409.

391 Brum, J, Catheline, S, Benech, N & Negreira, C. Shear elasticity estimation
392 from surface wave: The time reversal approach. *J Acoust Soc Am*, 2008,
393 **124**(6), 3377–3380.

394 Catheline, S, Souchon, R, Rupin, M, Brum, J, Dinh, AH & Chapelon, J-Y.
395 Tomography from diffuse waves: Passive shear wave imaging using low
396 frame rate scanners. *Appl Phys Lett*, 2013, **103**(1).

397 Choi, MJ, Guntur, SR, Lee, JM, Paeng, DG, Lee, KI & Coleman, A. Changes
398 in ultrasonic properties of liver tissue in vitro during heating-cooling cycle
399 concomitant with thermal coagulation. *Ultrasound Med Biol*, 2011, **37**(12),
400 2000–2012.

401 Chu, KF & Dupuy, DE. Thermal ablation of tumours: biological mechanisms
402 and advances in therapy. *Nature Reviews Cancer*, 2014, **14**(3), 199–208.

403 Deng, Y, Rouze, NC, Palmeri, ML & Nightingale, KR. Ultrasonic Shear Wave
404 Elasticity Imaging Sequencing and Data Processing Using a Verasonics
405 Research Scanner. *IEEE Trans Ultrason Ferroelectr Freq Control*, 2017,
406 **64**(1), 164–176.

407 Derode, A, Larose, E, Tanter, M & de Rosny, J. Recovering the Green's
408 function from field-field correlations in an open scattering medium (L). *J*
409 *Acoust Soc Am*, 2002, **113**(6), 2973.

410 Ebbini, ES & Ter Haar, G. Ultrasound-guided therapeutic focused ultra-
411 sound: Current status and future directions. *Int J Hyperthermia*, 2015,
412 **31**(2), 77–89.

413 Gallot, T, Catheline, S, Roux, P, Brum, J, Benech, N & Negreira, C. Passive
414 elastography: Shear-wave tomography from physiological-noise correlation
415 in soft tissues. *IEEE Trans Ultrason Ferroelectr Freq Control*, 2011, **58**(6),
416 1122–1126.

417 Gennisson, J-L, Rénier, M, Catheline, S, Barrière, C, Bercoff, J, Tanter,
418 M & Fink, Mathias. Acoustoelasticity in soft solids: Assessment of the
419 nonlinear shear modulus with the acoustic radiation force. *J Acoust Soc*
420 *Am*, 2007, **122**(6), 3211–3219.

421 Ghoshal, G, Kemmerer, JP, Karunakaran, C, Miller, RJ & Oelze, ML. Quan-
422 titative Ultrasound for Monitoring High-Intensity Focused Ultrasound
423 Treatment <italic>In Vivo</italic>. *IEEE Trans Ultrason Ferroelectr*
424 *Freq Control*, 2016, **63**(9), 1234–1242.

425 Giammarinaro, B, Zorgani, A & Catheline, S. Shear-Wave Sources for Soft
426 Tissues in Ultrasound Elastography. *IRBM*, 2018, **39**(4), 236–242.

427 Grasland-Mongrain, P, Zorgani, A, Nakagawa, S, Bernard, S, Paim, LG,
428 Fitzharris, G, Catheline, S & Cloutier, G. Ultrafast imaging of cell elas-
429 ticity with optical microelastography. *Proc Natl Acad Sci U S A*, 2018,
430 **115**(5), 861–866.

431 Lindop, JE, Treece, GMGee, AH & Prager, RW. Phase-based ultrasonic
432 deformation estimation. *IEEE Trans Ultrason Ferroelectr Freq Control*,
433 2008, **55**(1), 94–111.

434 Maloney, E & Hwang, JH. Emerging HIFU applications in cancer therapy.
435 *Int J Hyperthermia*, 2015, **31**(3), 302–309.

436 Montaldo, G, Tanter, M, Bercoff, J, Benech, N & Fink, M. Coherent plane-
437 wave compounding for very high frame rate ultrasonography and transient
438 elastography. *IEEE Trans Ultrason Ferroelectr Freq Control*, 2009, **56**(3),
439 489–506.

440 Nguyen, TM, Zorgani, A, Lescanne, M, Boccara, C, Fink, M & Catheline, S.
441 Diffuse shear wave imaging: toward passive elastography using low-frame
442 rate spectral-domain optical coherence tomography. *J Biomed Opt*, 2016,
443 **21**(12), 126013.

444 Parker, KJ, Doyley, MM & Rubens, DJ. Imaging the elastic properties of
445 tissue: the 20 year perspective. *Phys Med Biol*, 2011, **56**(1), R1–R29.

446 Pinton, GF, Dahl, JJ & Trahey, GE. Rapid tracking of small displacements
447 using ultrasound. *Proceedings - IEEE Ultrasonics Symposium*,2005, **4**(6),
448 2062–2065.

449 Righetti R, Kallel F, Stafford RJ, Price RE, Krouskop TA, Hazle JD & Ophir,
450 J. Elastographic characterization of HIFU-induced lesions in canine livers.
451 *Ultrasound Med Biol*, 2001, **25**(7):1099-113.

452 Sabra, KG, Conti, S, Roux, P & Kuperman, WA. Passive in vivo elastography
453 from skeletal muscle noise. *Appl Phys Lett*, 2007, **90**(19), 10–12.

454 Sanchez-Sesma, FJ. Retrieval of the Green's Function from Cross Correla-
455 tion: The Canonical Elastic Problem. *Bulletin of the Seismological Society*
456 *of America*, 2006, **96**(3), 1182–1191.

Sandrin, L, Catheline, S, Tanter, M, Hennequin, X & Fink, M. Time-Resolved Pulsed Elastography with Ultrafast Ultrasonic Imaging. *Ultrason Imaging* , 1999, **21**(4), 259–272.

Sanghvi, NT, Chen, WH, Carlson, R, Weis, C, Seip, R, Uchida, T & Marberger, M. Clinical validation of real-time tissue change monitoring during prostate tissue ablation with high intensity focused ultrasound. *J Ther Ultrasound*, 2017, **5**(1), 24.

Sapin-de Brosses, E, Gennisson, J-L, Pernot, M, Fink, M & Tanter, M. Temperature dependence of the shear modulus of soft tissues assessed by ultrasound. *Phys Med Biol*, 2010, **55**(6), 1701–1718.

Sapin-de Brosses, E, Pernot, M & Tanter, M. The link between tissue elasticity and thermal dose in vivo. *Phys Med Biol*, 2011, **56**(24), 7755–7765.

Tanter, M, & Fink, M. Ultrafast imaging in biomedical ultrasound. *IEEE Trans Ultrason Ferroelectr Freq Control*, 2014, **61**(1), 102–119.

Thittai, AK, Galaz, B & Ophir, J. Visualization of HIFU-Induced Lesion Boundaries by Axial-Shear Strain Elastography: A Feasibility Study. *Ultrasound Med Biol*, 2010, **37**(3):426-33.

Wu T, Felmlee JP, Greenleaf JF, Riederer, SJ & Ehman, RL. 2001 Assessment of thermal tissue ablation with MR elastography. *Magn Reson Med*, **45**(1):80-7.

Zhou, Y. Noninvasive Thermometry in High-Intensity Focused Ultrasound Ablation. *Ultrasound Quarterly*, 2017, **33**(4), 253–260.

479 Zorgani, A, Souchon, R, Dinh, AH, Chapelon, JY, Ménager, JM, Lounis, S,
480 Rouvière, O & Catheline, S. Brain palpation from physiological vibrations
481 using MRI. *Proc Natl Acad Sci U S A*, 2015, **112**(42), 12917–12921.

Figure Captions

Figure 1: Schematic display of the experimental set-up. A bovine liver sample is positioned in a sample holder in a water tank. The liver tissue is treated from above by a high-intensity ultrasound plane transducer, and imaged from the side using a high-frame-rate ultrasound scanner coupled to a linear transducer array.

Figure 2: Time-line diagram of a monitored experiment. The high-intensity ultrasound treatment and imaging are coupled so that the treatment continued for 1 min and was then paused for 7 s, to allow the imaging. This procedure was repeated every 1 min during the heating, and the imaging continued during the cooling.

Figure 3: Experimental results for samples 1 to 4. Shear-wave velocity maps before (left) and after (center left) the treatments. Center right: the average shear-wave velocities estimated during the treatments of the region of interest delimited by the white borders. Right: photographs of the treated samples.

Figure 4: Experimental results for samples 5 to 8. Shear-wave velocity maps before (left) and after (center left) the treatments. Center right: the average shear-wave velocities estimated during the treatments of the region of interest delimited by the white borders. Right: photographs of the treated samples.

Figure 5: Shear-wave particle velocity maps that were estimated successively for sample 1 at different times, for a frame rate of 600 Hz. Ex-

amples of waves are seen to pass from one side to the other of the tissue sample. The wave fronts are shown by the lines crossed by white arrows, which indicate the direction of their propagation.

Figure 6: Focal spot of the time-reversed signal calculated for a pseudo-source displayed as a white cross for sample 8 before (left) and after (right) the treatments. The size of the focal spot was increased by the high-intensity treatment.

Figure 7: Snapshot of the shear-wave velocity maps at different temperatures for sample 7. Softer borders can be seen, and are indicated by the dotted line.

Video Captions

Video 1: Shear-wave velocity maps for every temperature (given as the front title) for sample n°1.

Video 2: Shear-wave velocity maps for every temperature (given as the front title) for sample n°2.

Video 3: Shear-wave velocity maps for every temperature (given as the front title) for sample n°3.

Video 4: Shear-wave velocity maps for every temperature (given as the front title) for sample n°4.

Video 5: Shear-wave velocity maps for every temperature (given as the front title) for sample n°5.

Video 6: Shear-wave velocity maps for every temperature (given as the front title) for sample n°6.

Video 7: Shear-wave velocity maps for every temperature (given as the front title) for sample n°7.

Video 8: Shear-wave velocity maps for every temperature (given as the front title) for sample n°8.

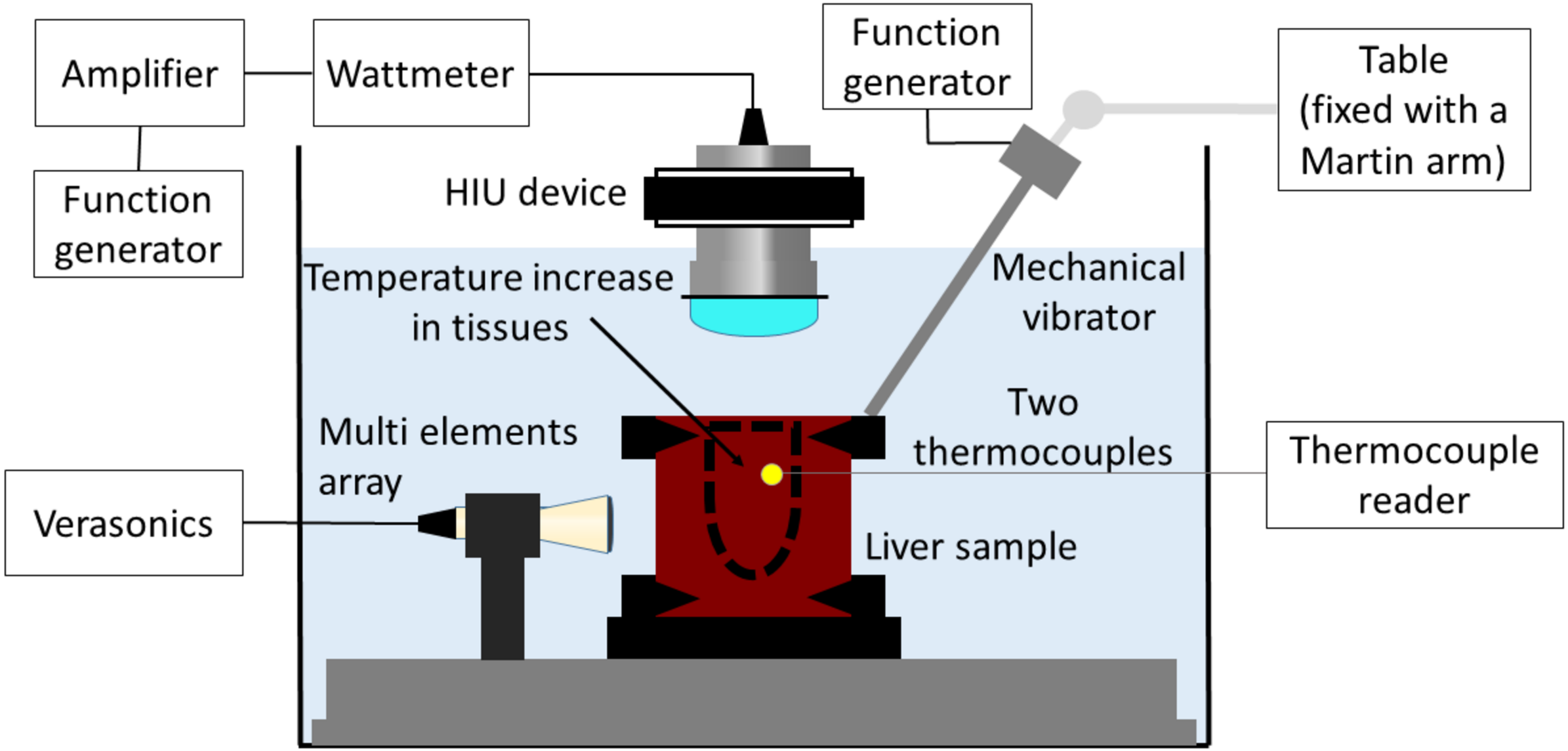
Amplifier
Wattmeter
Function generator
Table (fixed with a Martin arm)
Function generator
HIU device
Temperature increase in tissues
Mechanical vibrator
Two thermocouples
Multi elements array
Thermocouple reader
Verasonics
Liver sample

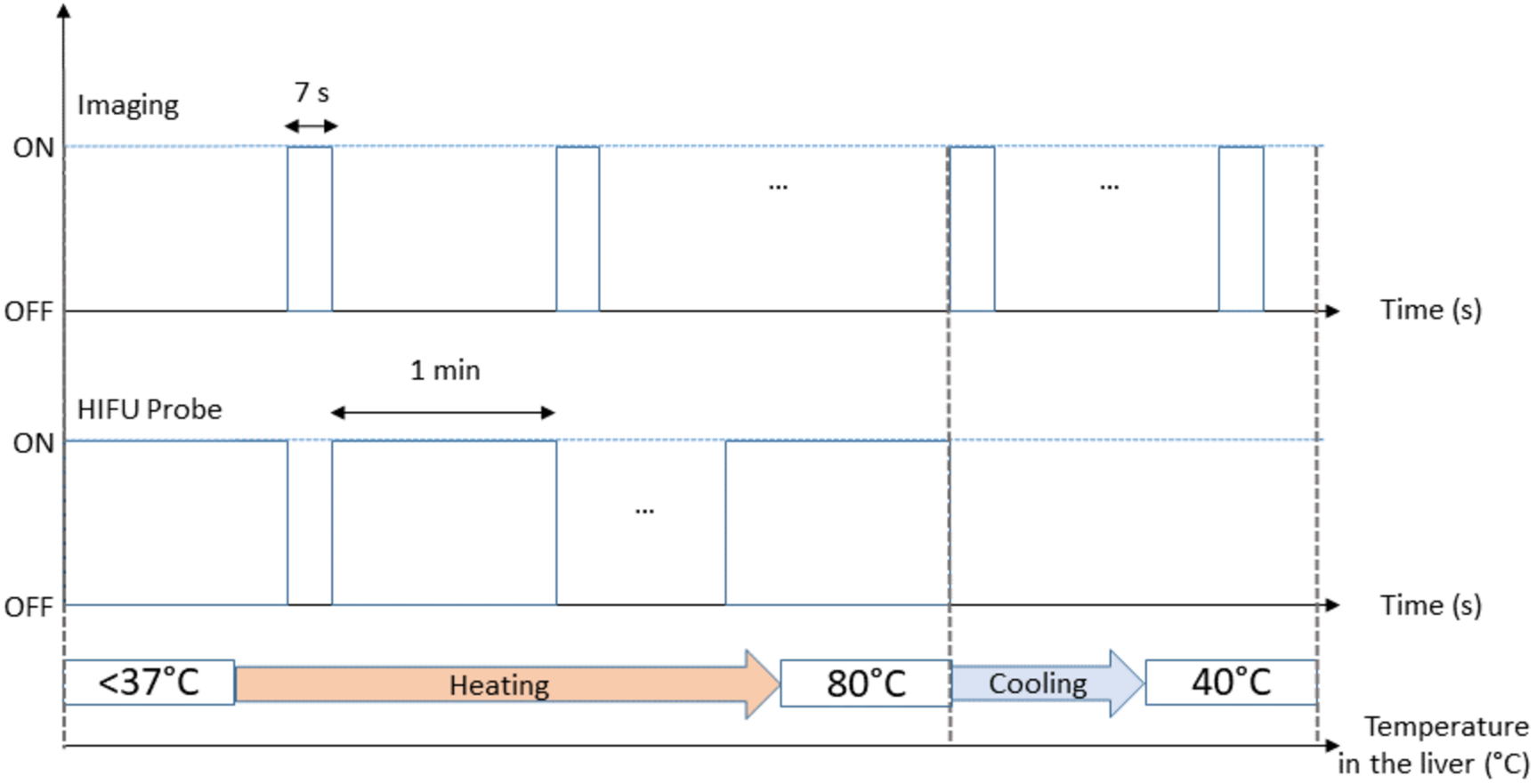
Imaging
7 s
ON
OFF
...
...
Time (s)
1 min
HIFU Probe
ON
OFF
...
Time (s)
<37°C
Heating
80°C
Cooling
40°C
Temperature
in the liver (°C)

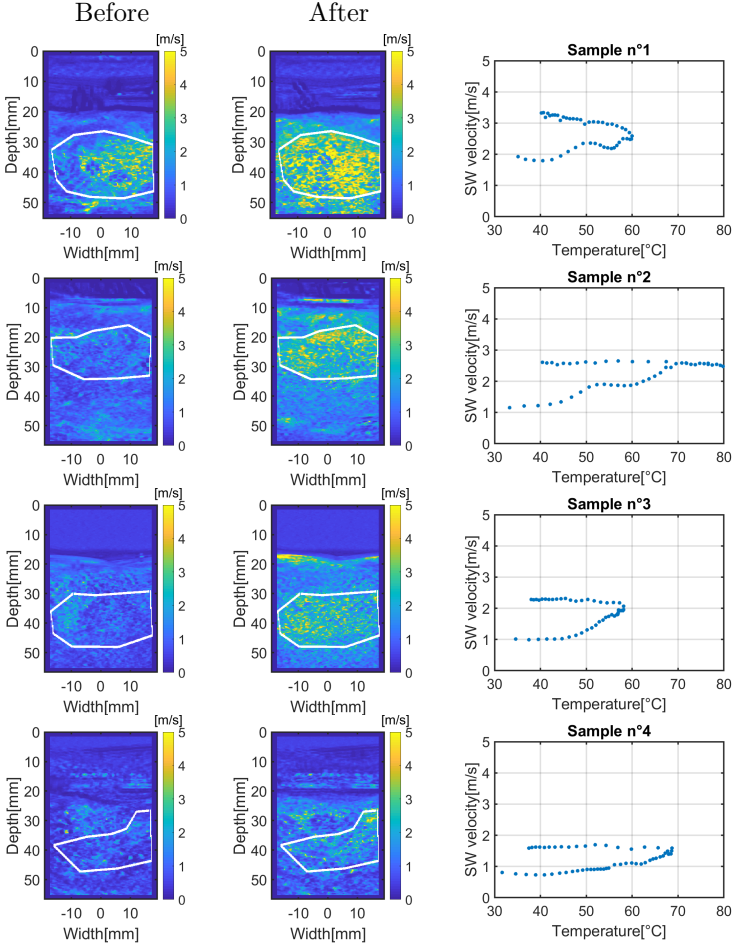
Before
After
Sample n°1
Sample n°2
Sample n°3
Sample n°4
Depth[mm]
Width[mm]
SW velocity[m/s]
Temperature[°C]
[m/s]

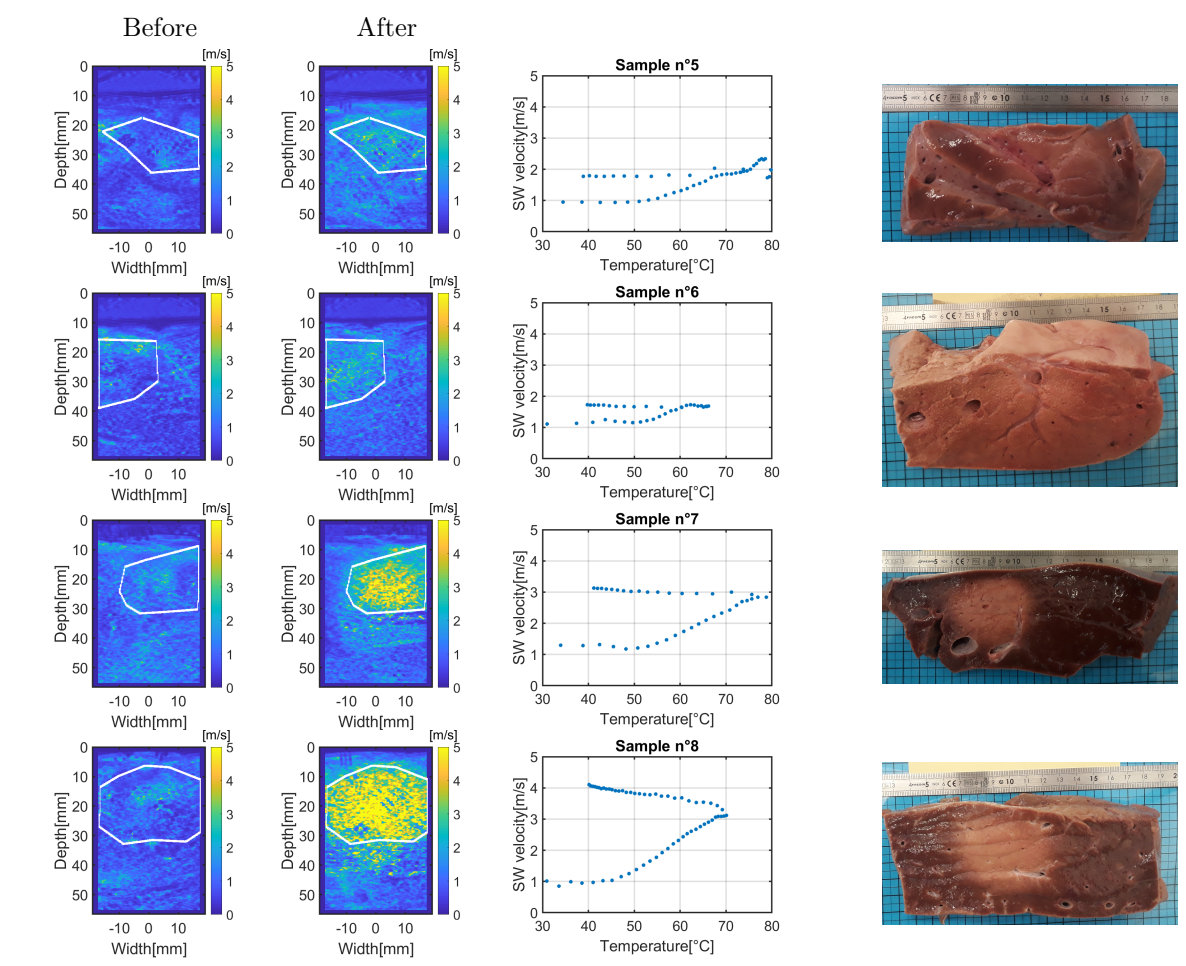
Before
After
[m/s]
Depth[mm]
Width[mm]
Sample n°5
Sample n°6
Sample n°7
Sample n°8
SW velocity[m/s]
Temperature[°C]

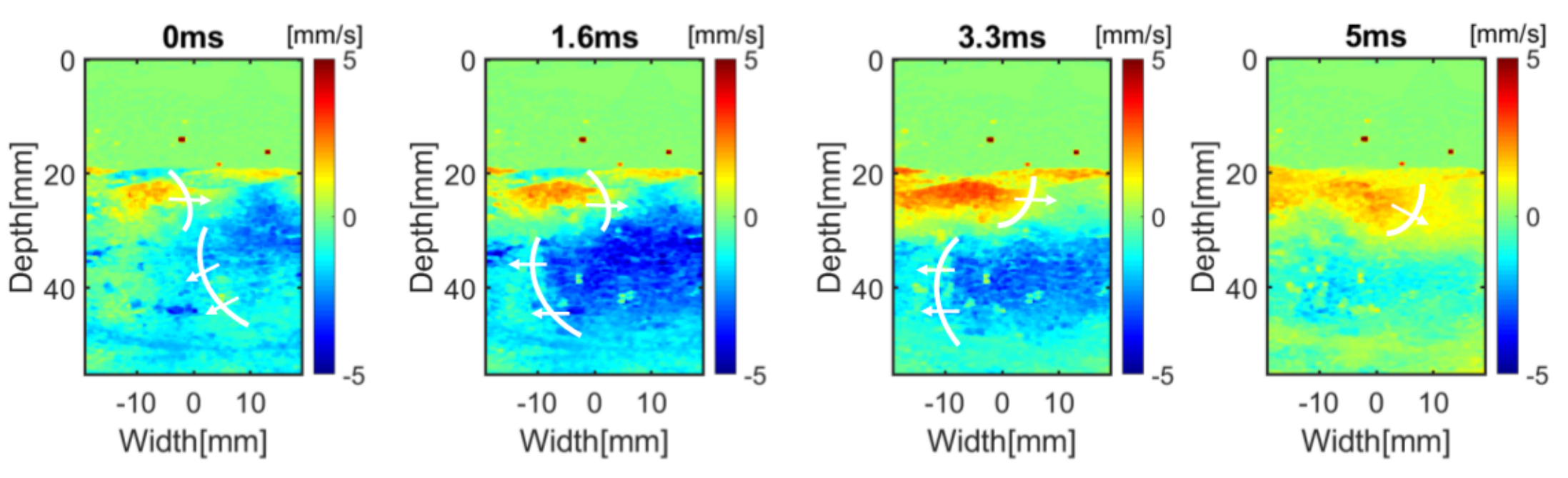
0ms
[mm/s]
5
0
-5
0
20
40
Depth[mm]
-10
0
10
Width[mm]
1.6ms
[mm/s]
5
0
-5
0
20
40
Depth[mm]
-10
0
10
Width[mm]
3.3ms
[mm/s]
5
0
-5
0
20
40
Depth[mm]
-10
0
10
Width[mm]
5ms
[mm/s]
5
0
-5
0
20
40
Depth[mm]
-10
0
10
Width[mm]

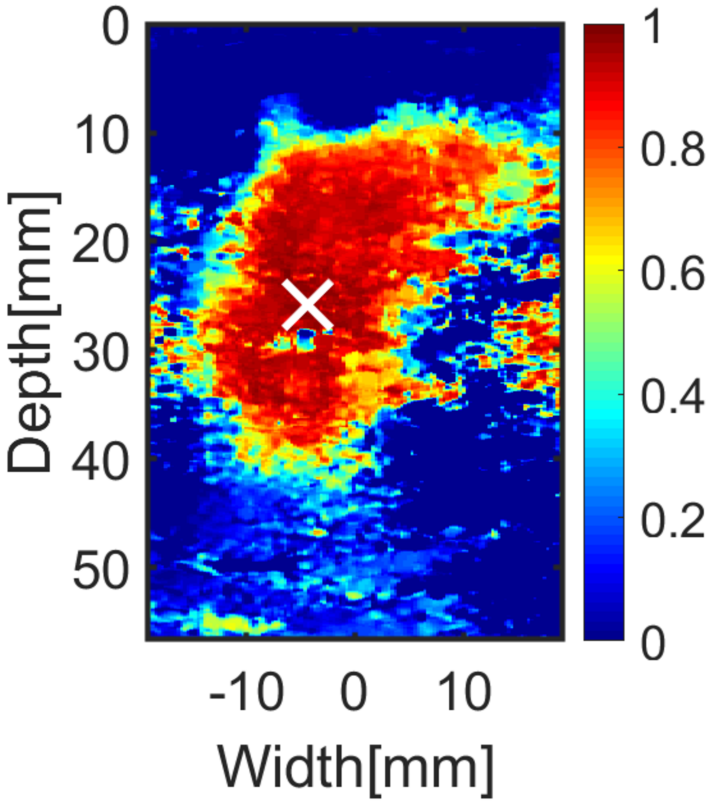
0
10
20
30
40
50
Depth[mm]
-10
0
10
Width[mm]
1
0.8
0.6
0.4
0.2
0

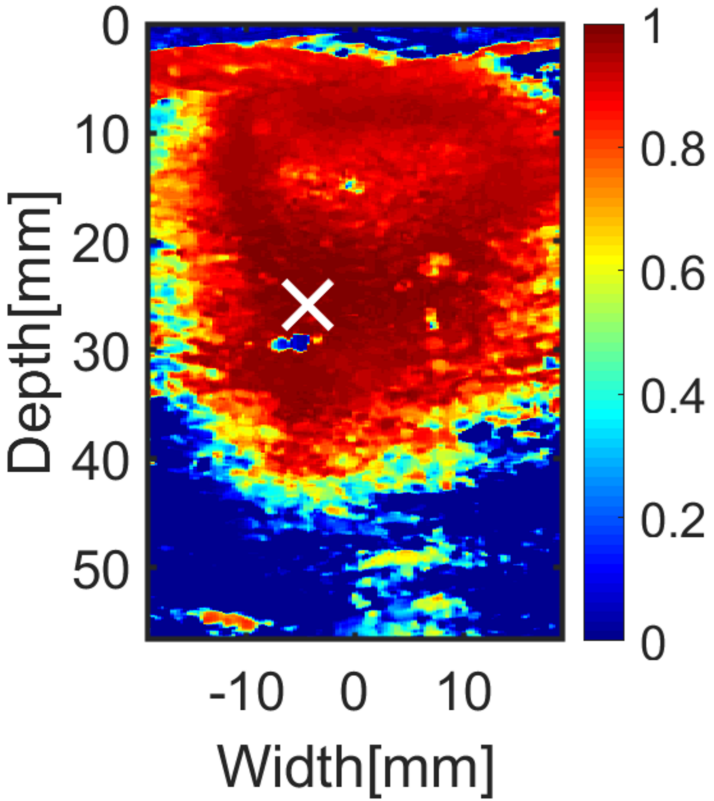
0
10
20
30
40
50
Depth[mm]
-10
0
10
Width[mm]
1
0.8
0.6
0.4
0.2
0

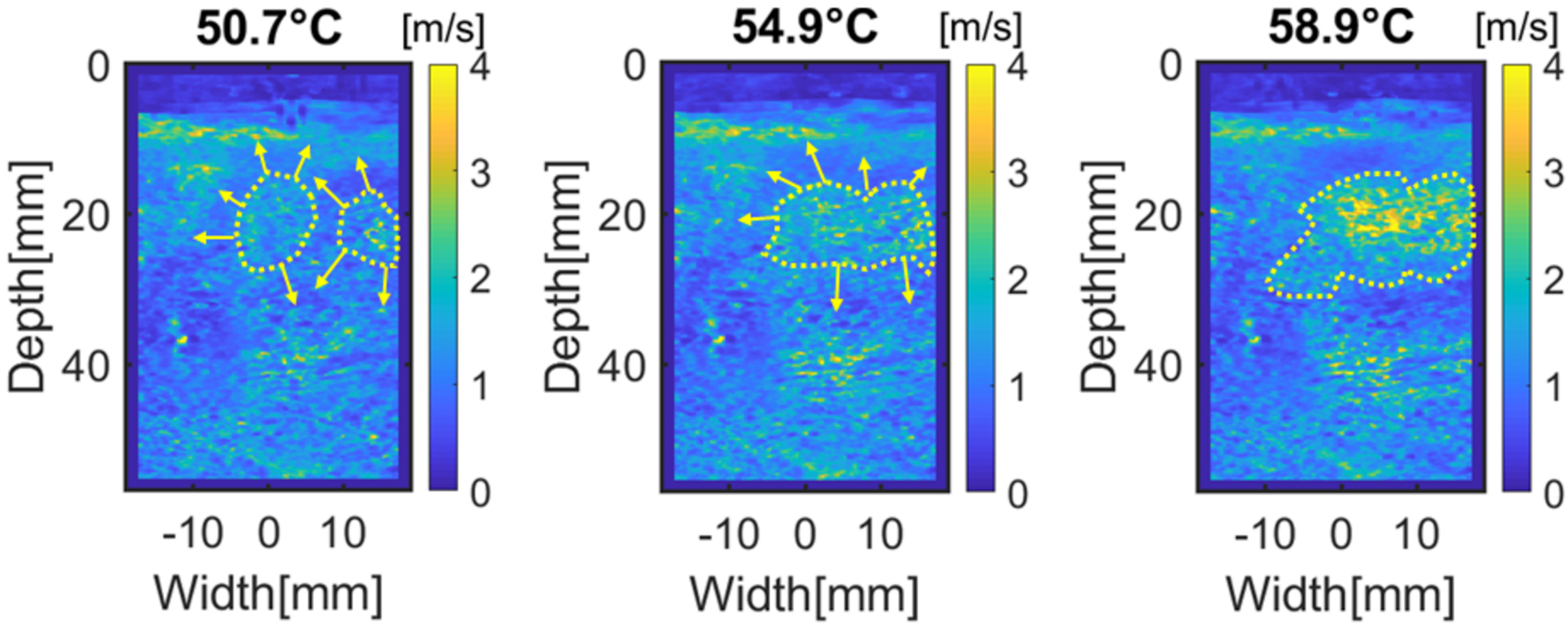
50.7°C
[m/s]
0
20
40
Depth[mm]
-10
0
10
Width[mm]
4
3
2
1
0
54.9°C
[m/s]
0
20
40
Depth[mm]
-10
0
10
Width[mm]
4
3
2
1
0
58.9°C
[m/s]
0
20
40
Depth[mm]
-10
0
10
Width[mm]
4
3
2
1
0